Lift characteristics of pitching NACA0015 airfoil due to unsteady forced surface inflation [†]

Ali Heydari[1,*] and Mahmoud Pasandideh-Fard[2]

[1]*Department of Mechanical Engineeing, Semnan branch, Islamic Azad University, Semnan, Iran*
[2]*Department of Mechanical Engineering, Ferdowsi University of Mashhad, Iran*

Abstract

The purpose of this work is to investigate the unsteady forced surface inflating (UFSI) effect on lift coefficient of a pitching airfoil. Thus, 2D unsteady compressible flow around a pitching airfoil is analyzed by means of coarse grid CFD (CGCFD) method and spring dynamic grids network. At first to validate the code for moving boundary cases, the predicted lift coefficient of pitching airfoil is compared with experiments. Simultaneously, the CGCFD results are compared with the RANS simulation. Then UFSI is added to the pitching airfoil. The effects of unsteady parameters such as the inflation amplitude and phase difference between pitching and inflation is investigated on lift and pressure coefficients of pitching airfoil. According to the results, UFSI, with zero degree phase difference between pitching and inflation, help to postpone the dynamic stall.

Keywords: Coarse grid CFD (CGCFD); Spring dynamic grid network; Forced surface inflation; Phase difference; Dynamic stall

---

1. Introduction

In recent decades, researches on smart materials such as piezo ceramics have been developed. Thus, the possibility has been provided for aerospace researchers to apply accurately controlled deformations on different parts of flying objects. Therefore, it can be useful to study the unsteady forced surface deformation effects on aerodynamic coefficients of flapping airfoils. It requires an unsteady analysis around the body and applying a valid and quick method to investigate accurately various unsteady parameters in a little time. Thus, in this work, coarse grid CFD (CGCFD) method is used to reduce significantly the computational time with acceptable results for the pitching airfoils [1, 2]. In this method, Euler equations are solved with coarse grid and no slip boundary conditions and using compressible surface vorticity confinement. Dietz et al. [2] used CGCFD technique to investigate unsteady flow around a pitching airfoil. They showed that this method predicts accurately the lift characteristics and estimates the dynamic stall well.

Approximately all efforts in the case of deformation are restricted in flexibility and aero elasticity in which aerodynamic forces lead to surface deformation that depends on flexibility and solidity of the wing material. This type of surface shape variation is called induced deformation. As instance, Aono [3] applied finite element method for elasticity and solved 3D Navier-Stokes equations simultaneously to model the flow around a flexible wing. They also experimentally investigated the effect of airfoil flexibility on aerodynamic forces and interaction of leading and trailing edge vortices. They showed that flexibility has an extreme effect on aerodynamics of flapping airfoils. Michelin and Llewellyn [4] used 2D potential flow to study inviscid flows around flexible pitching airfoils. They confirmed that the amplitude of trailing edge flapping has the maximum amount when a resonance occurs with natural and forced frequencies. Some of these resonances lead to a maximum thrust production. Shin and Kim [5] investigated the flow around flexible foils by using fluid structure interaction with immersed networks. This interaction is comprised of the effect of forces produced by oscillating airfoil and the surface deformation. They explained that the motion of flexible wings produces larger forces in comparing with rigid ones. Lian and Shyy [6] studied the effect of fixed airfoil flexibility on lift and drag coefficients and transition region. They showed that the flexibility has important effect on transition region, while the aerodynamic coefficients are similar to rigid fixed airfoils.

However, in some cases, it is possible that a forced deformation is applied to a surface. In this condition, a defined and controlled deformation is incurred to the surface which doesn't require elasticity analysis. Until present, the effect of forced

---

deformation is investigated less than induced one. But now, scientists could exert a defined and controlled deformation to the airfoil section with the aid of smart materials and piezo ceramics. This method is a practical but expensive which uses motive systems contain piezoelectric materials (Consist of Zink oxides, Plumb, Titanium and Zirconium). Piezoelectric can produce a controlled force for a various forced deformation by applying a specific voltage. These materials are used successfully in the construction of airfoil flaps [7, 8]. Piezoelectric motive systems have been used in flaps structure of helicopter blades by Clement et al. [9]. Munday and Jacob [10] could control the low Reynolds separation via camber oscillating by installation a piezoelectric actuator in the camber line.

Ysasi et al. [11] examined the wake structure generated by a deforming Joukowsky airfoil. They simulated the oscillatory motion of the fish by assuming a low Reynolds viscous incompressible flow around airfoils with a deformation that was expressed in terms of Jacobi elliptical functions. They showed that five wake structures were generated which were function of strouhal number and a dimensionless parameter related to deformation mode. These structures are used extensively in fish swimming for quick maneuvers. Lee and Su [12] experimentally analyzed the effect of systematic deformation of the trailing edge on aerodynamic forces in $Re = 2.5 \times 10^5$. These effects consisted of amplitude, the time of start and the frequency of trailing edge flapping. They showed that these factors make intense variations in oscillating hysteresis curvature of aerodynamic coefficients. The power of the vortex formation and separation from the leading edge is affected by the beginning time of the trailing edge motion. Therefore, the delay in the beginning time results in powerful changes in vortex strength. Ou and Jameson [13] simulated low Reynolds number flow around a plunging and pitching airfoil with deformation separately and simultaneously. For this purpose, a high order Navier-Stokes solver based on spectral difference method was used. They changed two parameters, the amount and the location of maximum curvature, to deform the shape of the section. Then, the conditions of maximum thrust generation were obtained. In recent investigations by Chandrasekhara et al. [14], it has been confirmed experimentally and numerically that the curve near the leading edge has much influence on the development of dynamic stall. Further, the local dynamic deformation of leading edge (That leads to local expansion of leading edge) is very impressive on the flow characteristics. Geissler and Trenker [15] also used numerically this type of deformation in the rotary blades.

Unsteady forced surface inflation (UFSI) is a type of deformation (Increasing thickness) which is forced to apply to the airfoil surface while pitching. The effect of UFSI on aerodynamic behavior of flyers has not been studied by researchers, yet. Probably, it has not been practically applicable till today. But with the development of science and technology in smart materials and Piezo ceramics, this type of deformation can be employed. Thus, the results of this paper can be helpful to study the effect of UFSI deformation on the flapping wing aerodynamic performance. To do this, UFSI is added to the surface of NACA0015 airfoil during pitching. After validation of the code, the effect of inflation amplitude and phase delay between pitching and inflation are investigated.

2. Numerical method

2.1 Governing equations

For the initial analysis, the general form of the Euler equations for a 2-D compressible inviscid flow is as following:

$$\frac{\partial W}{\partial t} + \frac{\partial E_i}{\partial x} + \frac{\partial F_i}{\partial y} = S \tag{1}$$

where W, is the flow component, F_i and E_i are inviscid flux vectors and S is compressible surface vorticity confinement source term, which will be presented later. Inviscid flux vectors are defined as below:

$$W = \begin{bmatrix} \rho \\ \rho u \\ \rho v \\ \rho e \end{bmatrix} \tag{2}$$

$$E_i = \begin{bmatrix} \rho(u - u_m) \\ \rho u(u - u_m) + \rho \\ \rho v(u - u_m) \\ (\rho e(u - u_m) + Pu) \end{bmatrix} ; F_i = \begin{bmatrix} \rho(v - v_m) \\ \rho u(v - v_m) \\ \rho v(v - v_m) + P \\ (\rho e(v - v_m) + Pv) \end{bmatrix}.$$

In which, ρ is density, u is the velocity in x direction and v is the velocity in y direction. u_m and v_m are the mesh velocity in x and y directions, respectively. e is the total energy and P is the pressure. In following equations, H and P are obtained, in which H is the stagnation enthalpy, c is the sound velocity and γ is the specific heat ratio.

$$H = E + \frac{p}{\rho} = \frac{c^2}{\gamma - 1} + \frac{u^2}{2} ; c^2 = \frac{\gamma P}{\rho} ; P = (\gamma - 1)\rho(e - \frac{u^2}{2}). \tag{3}$$

Eq. (1) can be expanded in one dimensional as following:

$$\Delta x \frac{dW_i}{dt} + F_{i+1/2} - F_{i-1/2} = 0 \tag{4}$$

$$F_{i+1/2} = \frac{1}{2}(F_{i+1} + F_i) - d_{i+1/2} \tag{5}$$

where $d_{i+1/2}$ is the dissipation term that is added to the equation to prevent oscillations and instabilities and it is the main reason of the artificial boundary layer growth. Some schemes have calculated this term as a function of flow gradients and conditions. In this work SCDS artificial dissipation scheme is used. (For more information, see Ref. [16])

In the case of no-slip boundary conditions for Euler equations with a coarse mesh, artificial viscosity produced by numerical dissipations leads to intense boundary layer growth which can be controlled by surface vorticity confinement. Compressible vorticity confinement (CVC) will be defined by adding a body force to the momentum equations and its correlated work to the energy equation in regions with high velocity gradient like vortical zones or surface boundary layer. It results in reduction or omission inherent dissipation related to the governing equations. The source term S is added to the Euler equations as CVC function (Eq. (1)). Its components are defined as follows [17, 18].

$$\vec{S} = (0 \quad \rho \vec{f}_b \cdot \hat{i} \quad \rho \vec{f}_b \cdot \hat{j} \quad \rho \vec{f}_b \cdot \vec{V}). \tag{6}$$

In which f_b is the body force per unit mass, and it balances the diffusion of the numerical errors and the conservation of momentum in the high velocity gradient regions. This force produces a velocity vector toward the center of the vortex in fully separated regions or toward the solid walls in regions near surfaces.

$$\vec{f}_b = -E_c \hat{n}_c \times \vec{\omega}. \tag{7}$$

E_c is the VC parameter that controls the power of confinement which is selected 0.06 with try and error to reach the best accuracy. VC can be applied in two distinct ways, field and surface confinement that depend on the definition of the unit vector n_c. Field confinement prevents numerical diffusion of convecting vortical structures and n_c is defined as the normalized gradient of the vorticity vector magnitude. For surface confinement, n_c is normal to the solid surfaces of the configuration. In this case, by adjustment of the confinement parameter, flows near body surface remains attached against an adverse pressure gradient. As a result, surface confinement can be considered as a simple implicit model for a turbulent boundary layer. When the numerical dissipation and VC are applied simultaneously, the right hand side of the Euler equations will be concluded as Eq. (8)

$$RHS = d_{i+1/2} + \rho E_c \, \omega_z \times \frac{\partial/\partial x \, |\omega_z|}{\left\| \nabla |\omega_Z| \right\|_{cons\,tan\,t}} \quad ; \omega_z = \frac{\partial v}{\partial x} - \frac{\partial u}{\partial y}. \tag{8}$$

The first term of this equation refers to numerical dissipation, and the second one is due to VC. Within the boundary layer ω_z and the VC term is negative that leads to reduction of numerical dissipation and artificial viscosity and prevents artificial boundary layer growth. Thus in the boundary layer, vorticity confinement becomes more important.

To study the effect of different parameters in different conditions, a quick and accurate scheme is required. As it was informed, CGCFD method is used in which Euler equations
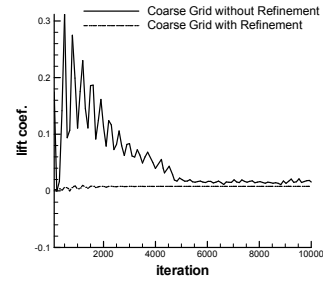

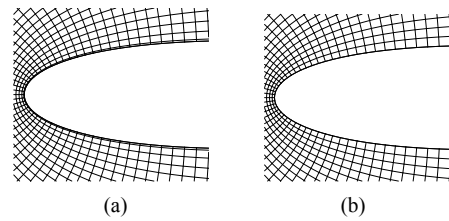Fig. 1. The effect of one mesh refinement near the wall on lift coefficient.

Fig. 2. Comparison of modified (a); and normal (b) coarse mesh.

are solved with coarse grid and no slip boundary conditions. This condition makes an extreme artificial boundary layer growth which can be controlled by surface vorticity confinement and becomes close to the real situation. As it is known, the time step of explicit unsteady solution and consequently the moving steps are functions of the smallest grid element size. In this method, the mesh is larger than very fine grids near walls suitable for boundary layer analysis. Therefore, the required running time for surface motion is reduced considerably compared to the viscous solution of Navier-Stokes equations even with the simplest turbulence model. By using this method, several moving oscillations can be modeled in just a few hours, while solving the viscous Navier–Stokes equations takes several days. To increase the speed of solution, dynamic spring grid analogy is used, too. These arrangements for speeding up the solution cause that a lot of effective parameters are evaluated in less time.

2.2 Mesh analysis and multi-zone adaptive grids

In CGCFD method, it is appropriate that just one element of inviscid network in the vicinity of the wall turns into smaller one without any changes in the other elements of the network. This mesh refinement leads to increasing the velocity gradients near the wall and according to Eq. (8) vorticity confinement near the wall will be stronger. It results in faster convergence, lower residuals, and omission of oscillations in results. The effect of one mesh refinement near the wall can be observed in Fig. 1. The results are related to a fixed symmetric airfoil at zero angle of attack.

In Fig. 1 lift coefficient versus iteration for both modified coarse grid and normal coarse mesh in zero angle of attack is shown. As it is obvious, mesh refinement near the wall re-
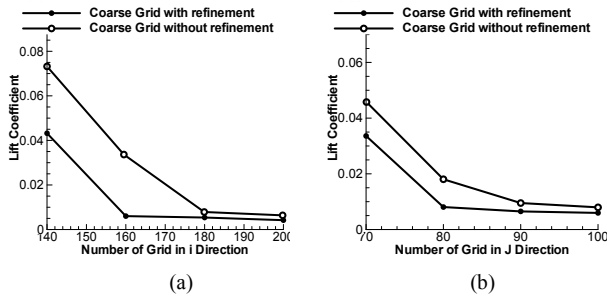
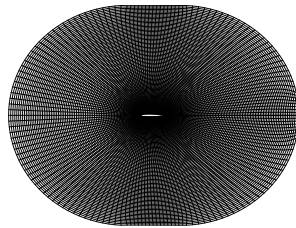Fig. 3. Grid independency in two directions: (a) j dir; (b) i dir.

Fig. 4. Selected grid for calculations.

duces the results oscillations and leads to convergence improvement. Modified and normal coarse grids are compared in Fig. 2.

To evaluate mesh independency, flow is passed over a fixed airfoil at zero angle of attack. The lift coefficient was calculated for both modified and normal coarse mesh and the results are shown in Fig. 3.

The selected grid is 90×160, because on one hand, lift coefficient variation is negligible with finer network and on the other hand computing costs are increased by finer grid with unimportant influences on the results. The selected grid is shown in Fig. 4.

In this work, when the boundary is moved or rotated the grid of computational domain is adjusted with boundary motion by using spring-analysis [19]. Applying this method effectively reduces the computational running time needed to find the solution. In this way, sides of the structured mesh are replaced by linear springs and reached equilibrium together at each step of movement. A logical definition is used for the spring constant. The stiffness of each spring is inversely proportional to its length. Thus, longer edges will be softer, while shorter ones will be stiffer; somewhat this assumption prevents the collision of neighboring vertices. If the displacements are large, the edge spring method cannot prevent the creation of nearly flat elements and it will lead to collapse the mesh networks. In order to avoid the possible collapse of grids network, the secondary linear springs has been also applied. However, the fine grids suitable for boundary layer most probably may collapse, specifically for the meshes adjacent to the walls.

To avoid this problem, a multi zone adaptive grid is designed for the computational domain which is divided in three zones. The first zone, that is adjacent to the body, is rotating

Table 1. Oscillating parameters for validation cases.

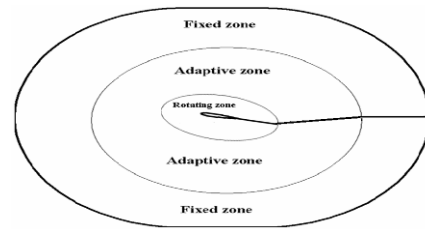| Case	α_m	α_0	k	Pitching center
Pitch1	0.88	4.33	0.133	0.25
Pitch2	4.02	4.33	0.133	0.25
Pitch3	8.99	2.08	0.1	0.25
Pitch4	12.95	4.04	0.04	0.25

Fig. 5. Multi zone adaptive grids.

with the boundary and is generated in each time step. The second one includes an adaptive zone in where the mesh points are adapted for each time step. Finally, the third zone (Outer region) is fixed and does not vary with time. It causes that grids in adaptive zone become coarser than near solid wall and collapsing will not occur during the motion. These zones are shown in Fig. 5.

2.3 Dynamic case study

In this paper the effect of unsteady forced surface inflation (UFSI) on lift characteristics of pitching airfoil is investigated. The pitching airfoil is NACA0015 with external flow of Mach number and Reynolds number equal to 0.3 and 2e6 respectively. For validation, the flow around a pitching airfoil is analyzed at various amplitudes and mean angles of attack (According to Table 1), and then the results are compared with experiments [20]. Also the results of CGCFD and RANS with Spalart-Almaras turbulence model are compared with each other. Eqs. (9) and (10) show the sinusoidal variation of the passing and effective angle of attack as:

$$\alpha(t) = \alpha_m + \alpha_0 Sin(kt) \tag{9}$$

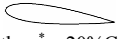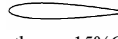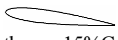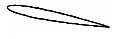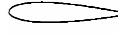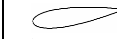$$\alpha_{eff}(t) = \alpha(t) + \frac{c\dot{\alpha}}{2U_\infty} . \tag{10}$$
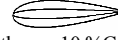
In which α_m, α_0 and $k = \omega c/U_\infty$ are the mean angle of attack, oscillation amplitude and reduced frequency, respectively and also $\alpha_{eff}(t)$ is the effective angle of attack [21].

The unsteady inflation is added to the surface during pitching motion. In this case, surface deformation is expressed by Eq. (11).

$$y_{(i,t)} = y_{(i,0)} + Ym_{(i)} Sin(kt + \varphi) . \tag{11}$$

In Eq. (11), $y_{(i,t)}$ is the coordinate of each node on the wall

Table 2. Summary of the inflated section in different phase difference at top, middle and bottom of pitching oscillation with 5% inflation.

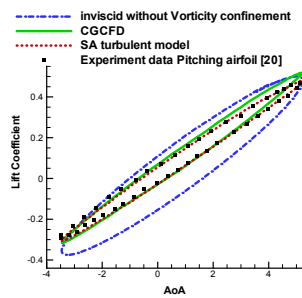| φ	At the top of oscillation	At the middle of oscillation	At the bottom of oscillation
0 °	$th_{max}{}^* = 20\%C$ (NACA0020)	$th_{max} = 15\%C$ (NACA0015)	$th_{max} = 10\%C$ (NACA0010)
90 °	$th_{max} = 15\%C$ (NACA0015)	$th_{max} = 10\ \%C\ \&$ 20 %C	$th_{max} = 15\%C$ (NACA0015)
180 °	$th_{max} = 10\%C$ (NACA0010)	$th_{max} = 15\%C$ (NACA0015)	$th_{max} = 20\%C$ (NACA0020)

* Maximum thickness

Fig. 6. Comparing the results of Lift coefficients versus angle of attack (AoA) ($k = 0.133$, $\alpha_0 = 4.33$ and $\alpha_m = 0.88$).

during the oscillation. $y_{(i,0)}$ indicates the primitive surface coordinates (The basic section NACA0015). $y_{m(i)}$ is the maximum thickness (Oscillation amplitude) of each node on the wall and φ is the phase difference between inflation and pitching motion. For instance, when it inflates gradually up to 5% chord it means that the section becomes NACA0020. A summary of the section shape in different φ is shown in Table 2. In all cases, the effect of inflation during the pitching is compared with the NACA0015 pure pitching (without deformation) results. Parameters which are investigated consist of amplitude of surface thickness ($y_{m(i)}$), mean angle of attack (α_m), phase difference between pitching and inflation (φ).

3. Results and discussion

3.1 Validation (Pure pitching)

First, the accuracy of the described method (Coarse grid CFD) is examined in comparison with the results of RANS with fine grid and one equation Spalart-Allmaras turbulence model and also the available experimental data in Ref. [20]. To perform this, the conditions, which have been demonstrated in Table 1, are added to the code, and the results are evaluated as follows.

As can be seen in Fig. 6, for $k = 0.133$, $\alpha_0 = 4.33$ and $\alpha_m = 0.88$, the lift coefficients obtained by CGCFD method, match well with the experiments, but a slight deviation at the top and bottom of the oscillation is perceived. The summary of calcu-

Table 3. Comparison of mean Lift coefficients ($k = 0.133$, $\alpha_0 = 4.33$ and $\alpha_m = 0.88$).

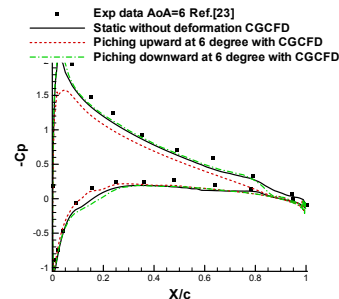| Method	$\overline{Cl}$	Time (Hour)
RANS	0.116	134
CGCFD	0.0995	4
Experiments	0.0804	

Fig. 7. Comparison of pressure coefficient on fixed and pitching airfoil at 6° angle of attack.
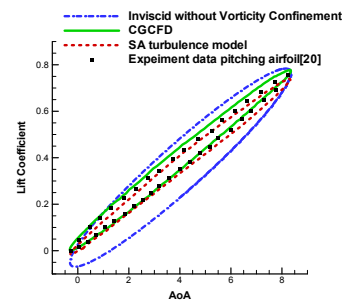

Fig. 8. Comparing the results of lift coefficients versus angle of attack (AoA) ($k = 0.133$, $\alpha_0 = 4.33$ and $\alpha_m = 4.02$).

lated average lift coefficient is illustrated in Table 3.

Pressure coefficients of fixed and pitching airfoil also should be compared with the experiments. For this purpose, the pressure coefficients of the fixed airfoil at angle of attack of 6° and also the pitching airfoil passing this angle in downward and upward motions are shown in Fig. 7. According to this figure, pressure coefficient curve related to down stroke is more extended than upstroke one. It is obvious that, in downward motion, lift coefficient is obtained higher than upward movement.

Fig. 8 indicates the results of lift coefficient versus angle of attack in comparison with experiments for $k = 0.133$, $\alpha_0 = 4.33$ and $\alpha_m = 4.02$. It shows the lift coefficient agree well with the experiments. In Table 4, the results of average lift coefficient are summarized.

In Table 4, the results of average lift coefficient are summarized.

In Fig. 9, the obtained lift coefficient is compared with the experiments for $k = 0.1$, $\alpha_0 = 2.03$ and $\alpha_m = 8.99$. This figure shows that at high angles without dynamic stall lift is predicted very close to the experiments. The results of average lift coefficient are also compared in Table 5.

Table 4. Comparison of mean lift coefficient ($k = 0.133$, $\alpha_0 = 4.33$ and $\alpha_m = 4.02$).

Method	$\overline{Cl}$	Time (Hour)
RANS	0.386	134
CGCFD	0.385	4
Experiments	0.348	

Table 5. Comparison of mean lift coefficients ($k = 0.1$, $\alpha_0 = 2.03$ and $\alpha_m = 8.99$).

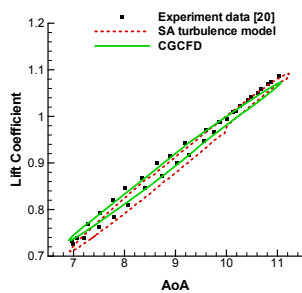| Method	$\overline{Cl}$	Time (Hour)
RANS	0.8993	144
CGCFD	0.9192	5
Experiments	0.9342	

Fig. 9. Comparing the results of Lift coefficient versus angle of attack (AoA) ($k = 0.1$, $\alpha_0 = 2.03$ and $\alpha_m = 8.99$).

As can be seen in Fig. 10, CGCFD method effectively and accurately estimates the dynamic stall which occurs at high angles of attack. Even the start and end point of separation and vortex shedding from the leading edge is predicted satisfyingly. Therefore, the results of this method can be trusted to estimate the dynamic stall process [2]. In Fig. 11, the dynamic stall and vortex shedding from leading edge at the top of the oscillation can be seen. In dynamic stall case, high-accuracy estimation of beginning and the end of dynamic stall procedure is also important.

To validate the vortex shedding obtained by the CGCFD method, it can be compared with Moulton's [22] results in the case of $\alpha = 10 + 10Sin(0.058t)$ on the top of the oscillation. Fig. 12 shows that the CGCFD method can predict the vortex shedding accurately.

According to the preceding consequences, RANS solution with fine grid and one equation Spalart-Allmaras turbulence model computes the hysteresis loops and average coefficients accurately, but a large computational time is required. The results of coarse grid CFD method are acceptable for lift coefficient and dynamic stall at low and high mean angles of attack. Because of very low required computational time, CGCFD method has a major advantage to be employed. Note that, one loop oscillation requires few hours computational time in this method, while it lasts for several days with a fully turbulent viscous analysis. Thus, coarse grid CFD method can
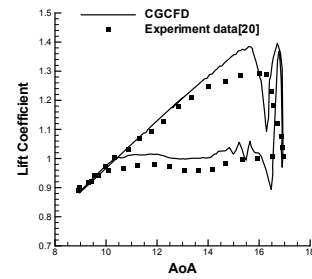

Fig. 10. Comparing the results of Lift coefficient versus angle of attack (AoA) ($k = 0.04$, $\alpha_0 = 4.02$ and $\alpha_m = 12.94$).
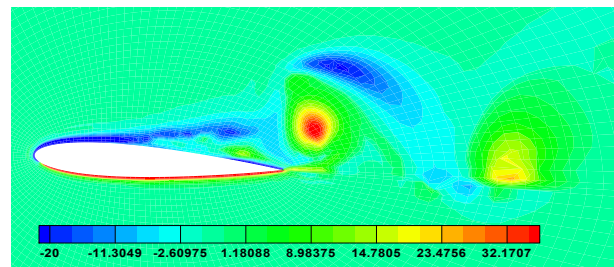

Fig. 11. Vorticity contour at the top of the oscillation with $k = 0.04$, $\alpha_0 = 4.02$ and $\alpha_m = 12.94$.
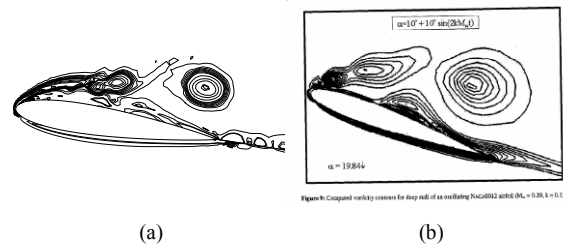

(a)   (b)

Fig. 12. Comparison of vorticity contour at the top of the oscillation (a) present work; (b) Moulton's results [22].

be applied as a quick and approximately accurate way to investigate the effects of different unsteady parameters on the lift coefficients in unsteady flapping airfoils.

3.2 Adding UFSI

3.2.1 Low angles effects

In this case the maximum surface thickness amplitude is selected 3%, 5% and 8% chord and the investigated mean angles of attack are 1º, 4º, 9º and 13º. To study the effect of phase difference (φ), 0º, 90º and 180º degrees of difference are preferred.

According to Fig. 13(a), for 1º mean angle, the effect of surface inflation on lift coefficient is negligible except at the top of the pitching motion. Maximum deviation at the top of the oscillation is related to $\varphi = 0º$. It leads to 5% decreasing in the maximum lift coefficient. Other phase differences have no effect on the pitching loop. In Fig. 13(b), the recent results are obtained for 4º mean angle of attack. The same consequences for lift coefficient are achieved.
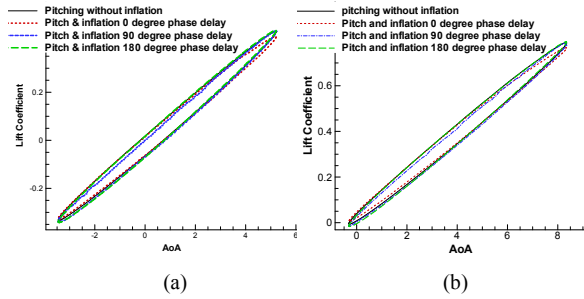
Fig. 13. The effect of phase difference between pitching and inflation on lift coefficients ($k = 0.133$, $\alpha_0 = 4.33$): (a) $\alpha_m = 0.88$; (b) $\alpha_m = 4.02$.

Fig. 14. The effect of phase difference between pitching and inflation on lift coefficients versus: (a) angle of attack; (b) non-dimensional time ($k = 0.1$, $\alpha_0 = 2°$ and $Ym_{max} = 3\%c$).
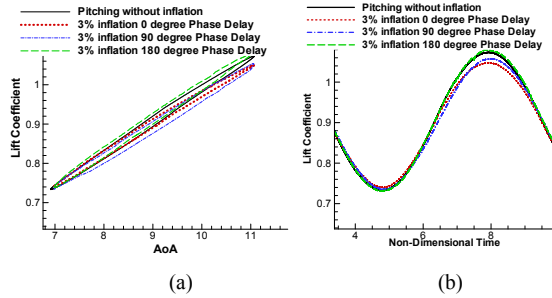

Fig. 15. The effect of phase difference between pitching and inflation on lift coefficients versus: (a) angle of attack; (b) non-Dimensional time ($k = 0.1$, $\alpha_0 = 2°$ and $Ym_{max} = 5\%c$).
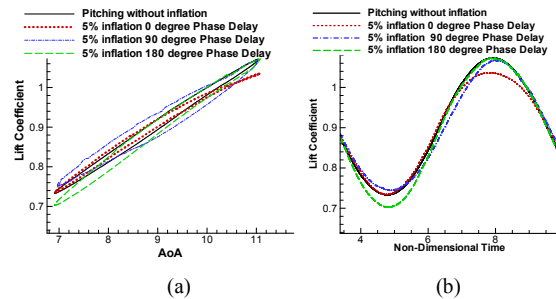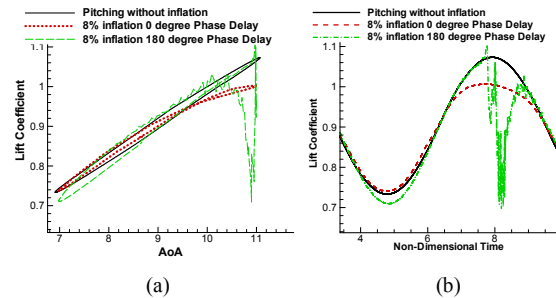

Fig. 16. The effect of phase difference between pitching and inflation on lift coefficients versus: (a) angle of attack; (b) non-dimensional time ($k = 0.1$, $\alpha_0 = 2°$ and $Ym_{max} = 8\%c$).
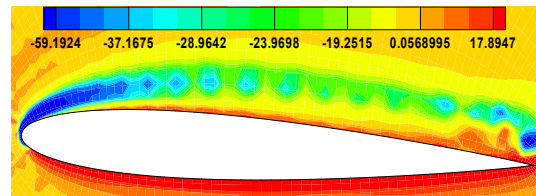

Fig. 17. Vorticity Contour at the top of the oscillation with $Ym_{max} = 8\%c$ and $\varphi = 180°$.

3.2.2 High angles effects

As it is observed, in low angles of attack the effect of UFSI during the pitching motion is negligible, but a major impression occurs in higher angles of attack. To investigate this effect, α_m is selected $9°$. In this angle, the maximum thickness (Ym_{max}), phase difference between pitching and inflation (φ) and reduced frequency (k) are varied. In Figs. 14-17 the amplitude of pitching angle and reduced frequency are selected $2°$ and 0.1, respectively. In Fig. 13, the effect of phase lag between pitching oscillation and surface inflation is investigated for 3% maximum thickness amplitude. As can be seen in this figure, UFSI is ineffective on the lowest lift coefficient. It means that the effect of airfoil thickness is negligible at the bottom of the oscillation. But it influences on the maximum lift coefficient. With enhancing in φ, increasing in greatest lift coefficient is achieved.

Thus, for $Ym_{max} = 3\%$, the maximum lift coefficient is reduced via $\varphi = 0°$ and $\varphi = 90°$ and it is enhanced by $\varphi = 180°$. Therefore, if the thickness at the top of the oscillation becomes greater, the maximum lift coefficient will be decreased, but if the thickness becomes less, it will be greater in comparing with pure pitching (without inflation). Fig. 15 shows the effect of φ in 5% maximum thickness amplitude. In this case, at the top of the oscillation, $\varphi = 0°$ reduces the maximum lift coefficient more than previous case, but it is already ineffective on the minimum one.

$\varphi = 90°$ results in widening the hysteresis lift curve and slightly increasing in smallest amount of lift coefficient without influence on the highest one. With higher Ym_{max} without

dynamic stall occurrence, $\varphi = 90°$ becomes more effective and leads to increasing in average lift coefficient. $\varphi = 180°$ leads to reduction of the lowest lift coefficient at the bottom of the oscillation without changing the highest one. Therefore, effectiveness of inflation on the minimum lift coefficient is achieved by enhancing the maximum thickness amplitude and phase lag simultaneously.

Fig. 16 characterizes that increasing simultaneously the maximum thickness amplitude and phase lag leads to intense reduction in lift coefficient. The sharp drop in lift coefficient is occurred due to vortex shedding from the leading edge. This experience is called dynamic stall. Vortex shedding from the leading edge of the airfoil at the top of the oscillation is shown in Fig. 17. In this point the airfoil has the maximum passing angle ($11°$), $\varphi = 180°$ and $Ym_{max} = 8\%c$. The vortex shedding is commenced from near the end of upstroke and it is extended to the middle of downward motion. Then the lift coefficient curve inclines to the hysteresis loop.

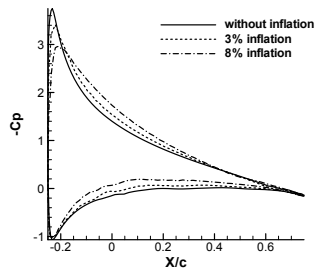Since the maximum variation of lift coefficient due to

Fig. 18. Pressure coefficient at top of the oscillation with $\varphi = 0^\circ$, $K = 0.1$ and $\alpha_0 = 2^\circ$.
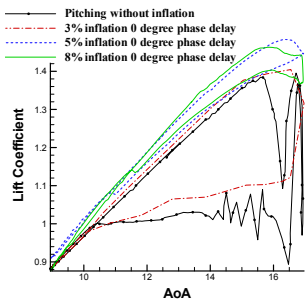

Fig. 19. The effect of maximum thickness amplitude on dynamic stall ($k = 0.04$, $\alpha_0 = 4.02^\circ$ and $\alpha_m = 12.94$).

inflation occurs at the top of the oscillation, to investigate the effect of UFSI on the pressure distribution, at this point of the oscillation, the pressure coefficient diagram over the airfoil is plotted in Fig. 18. φ has been selected 0° because dynamic stall does not occur even with $Ym_{max} = 8\%c$. It can be observed from the diagram that the pressure is reduced in the pressure side of the airfoil with inflation. But in the suction side, before the maximum pressure, it causes a reduction in pressure. The amount of the maximum pressure is reduced, too. After the maximum pressure point, it leads to increasing in pressure compared with the case without inflation. Increasing in φ leads to enhancement in the above differences with no inflation case.

3.2.3 Effects on dynamic stall

The above results indicate that phase differences $\varphi = 90^\circ$ and $\varphi = 180^\circ$ accelerate the occurrence of dynamic stall. But $\varphi = 0^\circ$ has the superior that it does not lead to dynamic stall even at high maximum thickness amplitudes. Since the maximum lift coefficient is decreased due to inflation with $\varphi = 0^\circ$, it may be able to delay the dynamic stall. Therefore, UFSI is added to the case Pitch4 in Sec. 3.1 (Fig. 10) which the dynamic stall occurred. The added inflation conditions are $\varphi = 0^\circ$ and $Ym_{max} = 5\%$ c.

Lift coefficient curves obtained from pure pitching oscillation and UFSI addition are compared in Fig. 19. The effect of the maximum thickness amplitude is also studied in this figure. As it is clear from this figure, the initial guess is true and adding inflation during the pitching oscillation with $\varphi = 0^\circ$ prevents leading edge vortex shedding and dynamic stall. It can be seen that the optimum value of the maximum thickness
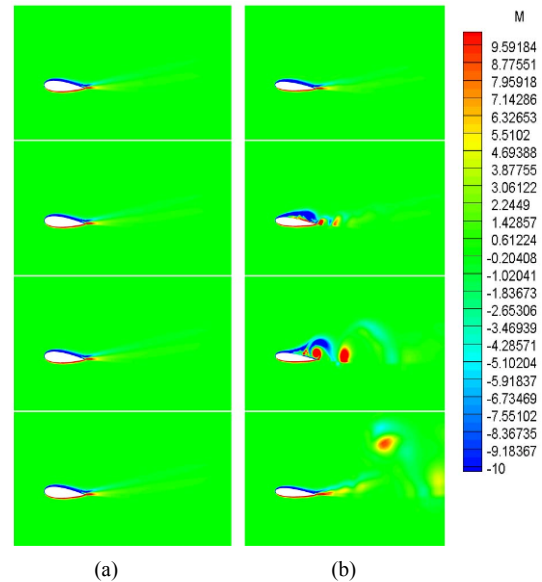

(a)   (b)

Fig. 20. Comparing vorticity contour at the top of the oscillation: (a) UFSI with $Ym_{max} = 5\%c$ and $\varphi = 0^\circ$; (b) pure pitching without inflation ($k = 0.04$, $\alpha_0 = 4.02^\circ$ and $\alpha_m = 12.94$).

amplitude is obtained for 5%c in which the average lift coefficient is the highest one in comparison with the other Ym_{max}.

In Fig. 20, the vorticity contour is shown near the top of the oscillation with $\varphi = 0^\circ$ and $Ym_{max} = 5\%c$ and it compares with pure pitching case. As can be seen, vortex shedding from the leading edge is eliminated. Thus, during the pitching oscillation, while the effective angle is reaching to the maximum value, if the thickness of symmetrical airfoils is enhanced the dynamic stall will be postponed.

4. Conclusion

CGCFD is a quick method which can be used to model the flow around oscillating airfoils with acceptable accuracy of pressure distribution and lift coefficient. It can also accurately predict the dynamic stall occurrence. With these capabilities, CGCFD is used to calculate the effect of different parameters such as the effect of surface inflation during the motion on unsteady flow around an oscillating airfoil. As it is clear from the article, the main effect of unsteady forced surface inflation (UFSI) during oscillation is the dynamic stall delay. It is found that, during the pitching, the thickness enhancement at high angles results to delay of dynamic stall. Also, the obtainable average lift coefficient is much higher than that with pure pitching. Further, in situations where intense reduction in lift is needed to control the flight, UFSI can be employed. More prefect consequences are investigated in the main text.

References

[1] J. Steinhoff, Y. Wenren, W. Dietz, M. Xiao and M. Fan, Computing blunt body flows on coarse grids using vorticity confinement, *Journal of Fluids Engineering*, 124 (2002)

876-886.

[2] W. Dietz, L. Wang, Y. Wenren, F. Caradonna and J. Steinhoff, The development of a CFD based model of dynamic stall, *American Helicopter Society 60th Annual Forum*, Baltimore, MD (2004).

[3] H. Aono, A computational and experimental study of flexible flapping wing aerodynamics, *48th AIAA Aerospace Sciences Meeting Including the New Horizons Forum and Aerospace Exposition,* 4-7 January, Orlando, Florida (2010).

[4] S. Michelin and S. G. Llewellyn, Resonance and propulsion performance of a heaving flexible wing, *Physics of Fluids*, 21 (2009).

[5] S. Shin and H. T. Kim, Numerical simulation of fluid-structure interaction of a moving flexible foil, *Journal of Mechanical Science and Technology,* 22 (2008) 2542-2553.

[6] Y. Lian and W. Shyy, Laminar-turbulent transition of a low Reynolds number rigid or flexible airfoil, *AIAA Journal,* 45 (7) (2007).

[7] F. K. Straub and D. J. Merkley, Design of a smart material actuator for rotor control, *Smart Materials and Structures*, 6 (1997) 26-34.

[8] A. Seifert, S. Eliahu, D. Greenblatt and I. Wygnanski, Use of piezoelectric actuators for airfoil separation control, *AIAA Journal*, 36 (1998) 1535.

[9] J. W. Clement, D. Brei, A. J. Moskalik and R. Barrett, Bench-top characterization of an active rotor blade flap system incorporating c-block actuators, *39th Structural Dynamics, and Materials Conference and Exhibit, AIAA*, 98 (1998) 2108.

[10] D. Munday and J. Jacob, Active control of separation on a wing with oscillating camber, *AIAA Journal of Aircraft*, 39 (1) (2002).

[11] A. Ysasi, E. Kanso and P. K. Newton, Wake structure of a deformable Joukowski airfoil, *Physica D*, 240 (2011) 1574-1582.

[12] T. Lee and Y. Y. Su, Unsteady airfoil with a harmonically deflected trailing-edge flap, *Journal of Fluids and Structures,* 27 (2011) 1411-1424.

[13] K. Ou and A. Jameson, Optimization of flow past a moving deformable airfoil using spectral difference method, *41st AIAA Fluid Dynamics Conference and Exhibit,* Honolulu, Hawaii, AIAA (2011) 3719.

[14] M. S. Chandrasekhara, M. C. Wilder and L. W. Carr, Control of flow separation using adaptive airfoils, *AIAA 35th Aerospace Sciences Meeting,* Reno, NV (1997).

[15] W. Geissler and M. T. Trenker, Numerical investigation of dynamic stall control by a Nose-Drooping device, *American Helicopter Society,* San Francisco, CA (2002) 23-25.

[16] A. Jameson, W. Schmidt and E. Turkel, Numerical solutions of the euler equations by finite volume methods using Runge-Kutta time-stepping schemes, *AIAA Journal*, 81 (1981) 1259.

[17] J. Steinhoff, Vorticity confinement: A new technique for computing vortex dominated flows, *Frontiers of Computational Fluid Dynamics*, D.A. Caughey and M.M. Hafez eds., J. Wiley & Sons (1994).

[18] W. E. Dietz, Application of vorticity confinement to compressible flow, *42nd AIAA Aerospace Sciences Meeting and Exhibit,* Reno, Nevada, 5 - 8 January (2004).

[19] K. Nakahashi and G. S. Deiwert, Three dimensional adaptive grid method, *AIAA Journal*, 24 (1999) 948-954.

[20] R. A. Piziali, An experimental investigation of 2D end 3D oscillating wing aerodynamics for a range of angle of attack including stall, *NASA Technical Memorandum*, *No. 4632. Ames, CA: NASA 4632*, Chalmers University of Technology (1993).

[21] D. Rival and C. Tropea, Characteristics of pitching and plunging airfoils under dynamic-stall conditions, *Journal of Aircraft*, 47 (1) (2010).

[22] M. Moulton and J. Steinhoff, A technique for the simulation of stall with coarse-grid CFD, *AIAA-00-0277* (2000).

Ali Heydari was born in Mashhad, Iran, in 1983. He received a BS degree in Mechanical engineering, in 2006, and an MS degree in Energy Conversion, in 2006, from the Mechanical Engineering Department of Ferdowsi University, Iran, where he got the Ph.D. degree too in the same subject. His research interests include CFD, unsteady aerodynamics, boundary layer characteristics and solar energy, and he is currently working as a faculty member (Assistant professor) in the Mechanical Engineering Department at the Islamic Azad University of Semnan, Iran.